Journal of
Micro/Nanolithography, MEMS, and MOEMS

SPIEDigitalLibrary.org/jm3

Homogeneous one-dimensional optical lattice generation using a digital micromirror device-based high-precision beam shaper

Jinyang Liang
Rudolph N. Kohn, Jr.
Michael F. Becker
Daniel J. Heinzen

SPIE

Homogeneous one-dimensional optical lattice generation using a digital micromirror device-based high-precision beam shaper

Jinyang Liang
University of Texas at Austin
Department of Electrical and Computer Engineering
Austin, Texas 78712
E-mail: jinyang.liang@mail.utexas.edu

Rudolph N. Kohn, Jr.
University of Texas at Austin
Department of Physics
Austin, Texas 78712

Michael F. Becker
University of Texas at Austin
Department of Electrical and Computer Engineering
Austin, Texas 78712

Daniel J. Heinzen
University of Texas at Austin
Department of Physics
Austin, Texas 78712

Abstract. A homogeneous one-dimensional optical lattice is demonstrated by using a high-precision beam shaper based on a digital micromirror device (DMD) with an imaging system containing a pinhole low-pass filter (LPF). This system is capable of producing a high-quality flattop beam profile to form a standing-wave optical lattice with a 50×50 μm^2 flattop region. The periodic potential generated by the optical lattice confines ultracold atoms in Bose-Einstein condensate experiments. We conducted beam shaping tests at several wavelengths by implementing various coherent and incoherent light sources in the visible and infrared wavelength ranges. Experiments produced flattop and other well-controlled beam profiles with 0.2% to 0.26% root-mean-square (RMS) error after applying a digital LPF and nearly flat phase. Several concerns for the system design are presented. First, the energy requirement was determined by power conversion analysis and DMD diffraction efficiency simulation. In addition, a LabVIEW program was written to accelerate the speed of the iterative process for beam profile refinement. Finally, various camera calibrations improved the measurement accuracy. We achieved a 1.25% RMS error flattop beam with diameter of 70.4 μm at the atoms' plane. Other beam profile measurements in different diagnostic planes demonstrated a good intensity uniformity of the optical lattice. [DOI: 10.1117/1.JMM.11.2.023002]

Subject terms: optical lattice; beam shaping; spatial light modulators.

Paper 11168P received Dec. 1, 2011; revised manuscript received Feb. 9, 2012; accepted for publication Mar. 9, 2012; published online May 21, 2012.

1 Introduction

Recent breakthroughs for Bose-Einstein condensates (BEC) in optical lattices[1,2] have provided a novel approach to understand characteristics of modern materials, such as superconductors, spin systems, and carbon nanotubes. Precise control of the optical lattice enables the emulation of strongly-interacting, many-body systems for both bosons and fermions. Such systems are realizations of the Hubbard or Bose-Hubbard model, which describes a system of bosons or fermions in a lattice potential, and has been studied intensely over the past decade. In quantum emulation, ultracold atoms confined by an optical lattice are trapped at the intensity maxima or minima depending upon the specific electronic dipole transition energy within an atom with respect to the laser frequency. The potential well depth, determined by the power of optical lattice beams, controls the phase of the quantum gas, with atoms either moving freely from site to site or with definite numbers of atoms held in each site.

An optical lattice can be constructed by using either coherent or incoherent light. Lasers are commonly used to create 3-D optical lattices for ultracold atom experiments.[3] On the other hand, thin or 2-D optical lattices can be formed by direct projection of an incoherent light pattern onto the atoms plane or by coherent standing waves. An incoherent light source has improved the resolution and sensitivity of the quantum gas microscope by generating smoother potentials with less stray light, and the potential shape has been further modified by an additional incoherent beam that is added to the lattice potential in order to flatten lattice inhomogeneities.[4]

Our main interest is to form a highly uniform optical lattice for quantum emulators using Bose-Einstein condensates of ultracold atoms. A high-quality flattop beam is desired for this application because of its ability to produce a spatially homogeneous potential for ultracold atoms with errors or fluctuations well below 1% root-mean-square (RMS) error and approaching 0.1% RMS error if possible. Such precise flattop beams have other useful applications, such as improving the sensitivity of interferometric gravity wave detectors.[5] Our objective is to generate a flattop beam with intensity flatness over the central region. The transition regions at the edge of the beam are not our primary interest because most of the ultracold atoms are trapped near the lowest potential at the center of the beam. In addition, we can give up some degree of conversion efficiency from the Gaussian input to flattop output in order to achieve high-precision beam control. Finally, a uniform-phase wave front over the flattop area is necessary to ensure spatial homogeneity of the optical standing-wave field.

A high-quality flattop profile can be produced by using various beam-shaping techniques.[6,7] Well-controlled beam shapes can be generated by different passive approaches, such as the diffractive phase plate,[8,9] refractive aspheric lens pair,[10,11] or binary-transmissive metal mask.[12] However,

0091-3286/2012/$25.00 © 2012 SPIE

these static methods cannot adjust for variations in input beam profiles due to imperfect optical systems or produce different types of output beam profiles on demand. Spatial light modulators (SLMs), on the other hand, provide a programmable modulation of phase and/or amplitude.[13,14] We employed a Texas Instruments (TI) digital micromirror device (DMD) binary-amplitude spatial light modulator (SLM) as an active adaptive transmissive mask to design arbitrary beam shapes.[15,16] Previous work by Sumriddetchkajorn[17] used a DMD to demonstrate a programmable optical beam shaper. The output beam profile was controlled by time-varying binary pulse-width modulation of the pixel mirrors, meaning that each DMD mirror was dithered during the beam shaping process based on the digital control signal. This approach is similar to DLP display technology and is not directly suitable for our BEC experiment. Because the ultra-cold atoms are sensitive to time variations of intensity, the optical trap would be broken by a time-changing DMD pattern. As a result, we can only project a static binary pattern on the DMD to generate the desired beam profile at the output plane. In this paper, we demonstrate a homogeneous one-dimensional (1-D) optical lattice by using a DMD-based high-precision beam shaper containing a two-arm telescope system with an adjustable pinhole low-pass filter (LPF). This system is expected to generate a high-quality homogeneous 1-D optical lattice by converting a raw quasi-Gaussian input to flattop beam with a high degree of intensity flatness and a reasonably uniform phase. We create a 1-D optical lattice at the correct size for cold atom experiments with RMS error below 0.3%. This unprecedented low error level is approaching our target of 0.1% for the cold atom experiments. In addition, we demonstrate the ability to shape beams of different wavelengths as well as fast and automatic control of the beam shaping system.

In the next section, we describe our method to produce flattop beams and the important factors that should be considered. Section 3 summarizes high-precision beam shaping using different light sources and compares results with respect to image precision and power conversion efficiency. Section 4 presents the experimental results for homogeneous 1-D optical lattices formed using the LabVIEW automated system. We describe the system calibration based on white-field measurements and scaling parameters between the DMD and measurement camera. Intensity uniformity of beam profiles at different imaging planes in the system is compared to examine the quality of the generated optical lattice. A summary concludes the paper in Sec. 5.

2 Experimental Method and SLM Selection

2.1 *Experimental Setup*

Figure 1 shows the optical layout of the homogeneous 1-D optical lattice test bench configured to produce a standing-wave optical lattice of the correct size for cold atom experiments. The input quasi-Gaussian beam is expanded and collimated by a 5× telescope to best fit the DMD size. No spatial filtering is conducted for the input light. A pinhole, functioning as a spatial low-pass filter, is placed at the back focal plane of the first lens (f1). The pinhole diameter varies from 610 to 1200 μm, depending upon the input light source. The DMD, camera, and other optical elements are all perpendicular to the optical axis.

The light passing through the pinhole is split into the image feedback arm (f3) and optical lattice arm (f2). The telescope in the image feedback arm (f1 and f3) uses 300 and 250 mm or 500 and 400 mm focal length lenses to image the DMD with a magnification of $-5/6$ or $-4/5$. A windowless Spiricon charge coupled device (CCD) camera is placed at various diagnostic planes to monitor beam profiles. In the optical lattice arm, the beam size is reduced by the telescope (f1 and f2) and a following imaging lens (f4). The optical lattice beam is then retro-reflected by a lens-mirror combination (f5 - m1) to form the 1-D standing-wave optical lattice in a region smaller than 50 μm on a side.

2.2 *Pattern Generation Process*

The amplitude diffraction function for the DMD is calculated based on the desired target function and the input quasi-Gaussian beam profile that is accurately measured by a windowless Spiricon camera (4.4 μm pixel size). It is then converted to the binary DMD pattern by a digital halftoning error diffusion algorithm[18] followed by digital pattern refinement. The DMD pattern is further refined based on repeated accurate images of the output beam profile followed by pixel adjustments based on suppressing successively smaller peaks and valleys in the difference between the measurement and target profiles.

In order to separate the error introduced by the optical system from that introduced by coherent speckle and camera noise, a digital low-pass filter with an equivalent cutoff

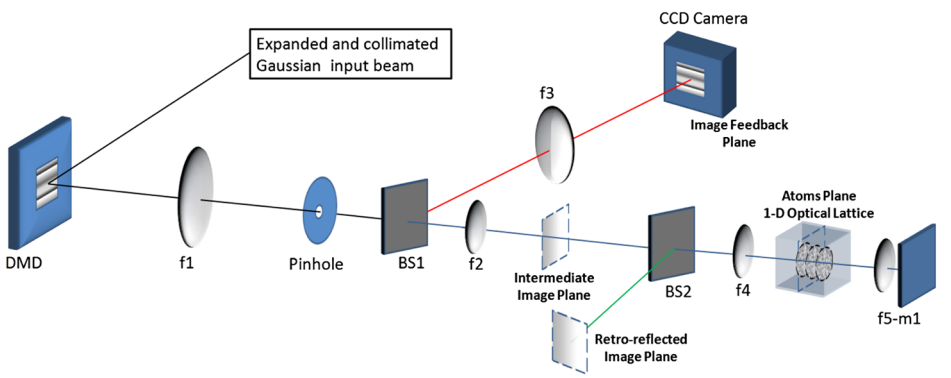

Fig. 1 Optical layout of the homogeneous 1-D optical lattice test bench. The first beam splitter (BS1) separates light into the image feedback arm (red) and the optical lattice arm. The second beam splitter (BS2) forms the retro-reflected image plane (green).

frequency to the pinhole in the experiment was applied to the camera images. The spatial frequencies that were eliminated by the digital LPF were more than 35 dB below the peak of the spatial frequency spectrum of a measured flattop beam profile. Thus, the major frequency components of the beam profile were not affected.

2.3 *Flattop Beam Generation Considerations*

Several factors are considered to insure a high-quality flattop beam. First, the DMD has exceptional advantages for our application. Because ultracold atoms are sensitive to intensity fluctuation of the optical field, uncontrolled time variation is unacceptable in the optical lattice. As a binary amplitude spatial light modulator, each micromirror in the array can be electrostatically latched to $\pm 12°$ to ensure steady, precise, and repeatable performance. This is especially good for static image formation. In addition, an 8th order Super-Lorentzian profile, $SL(x, y)$, was used as the target flattop function in the work reported here and is given by

$$\mathrm{SL}(x, y) = \mathrm{SL}_0 \left[1 + \left| \frac{\sqrt{(x - x_o)^2 + (y - y_o)^2}}{r_{\mathrm{SL}}} \right|^8 \right]^{-1}, \qquad (1)$$

where SL_0 and r_{SL} are the amplitude and width of the beam profile centered at (x_o, y_o). Like other higher order Gaussian or Lorentzian beam shapes, this profile has a flattop central region and a smooth transition to zero irradiance at the edge. These functions have a narrow spatial frequency bandwidth compared to the top-hat or perfect circle function.

The narrow spatial frequency distribution is preserved for binary modulation by using the error diffusion algorithm[19] with the pinhole low-pass filter. This adaptive digital halftoning technique not only enables us to shape beams having arbitrary input and output combinations with high precision, but it also generates a gray-preserved quasi-random binary pattern with a spatial frequency spectrum that minimizes noise at low spatial frequencies. This generated binary pattern is an ideal input to the spatial filter whose cutoff frequency is selected to be just sufficient to pass the target beam spectrum and filter out the high spatial frequency content from the individual pixels.

3 Summary of Previous Results

One important aspect of our previous work is the demonstration of the flexibility of our method to be applied to a wide range of light sources of different wavelengths and different degrees of coherence. Wavelength selection will, of course, be important for the experimental application, but it also determines the diffraction order and conversion efficiency of the DMD system. Source coherence and linewidth affect the speckle noise present in both the precision imaging camera and the optical lattice. We will see that incoherent sources can form flattop beams of lower RMS error due to speckle reduction, but there is a limit to the allowed source linewidth because the system is diffractive and functions as a spectrometer for a broad-band input. In addition, since the optical lattice can be produced using either coherent or incoherent light sources as described earlier, it is necessary to compare the quality of generated flattop beam profiles using these different light sources. As the first step toward homogeneous 1-D optical lattice generation, we tested beam shaping performance at the image feedback arm. Recently, we demonstrated flattop and other beam profiles with 0.81% to 1.12% root-mean-square (RMS) error for a raw camera image and nearly flat phase.[15,16,20]

3.1 *Coherent Laser Beam Shaping*

We used a 633 nm He-Ne laser and 1064 nm single-mode fiber laser as coherent light sources for laser beam shaping. The pinhole size was adjusted according to the best beam shaping performance for each light source. Initial experimental results showed that a noisy Gaussian input was converted to a flattop laser beam with 1.5% RMS error over the entire flattop area.[15] Using iterative pattern refinement, we generated various types of flattop beams, including circular and square cross section flattop beams and linearly tilted beam profiles. These results verified that iterative refinement reduced the RMS error of from more than 1.5% to 1% at 633 nm and 1.12% at 1064 nm.[16] The remaining error after the digital LPF was between 0.23% and 0.7% RMS depending on the performance of the DMD pattern design algorithm. The remaining error of 0.23% was very close to that calculated to come from design algorithm imperfections, residual low-frequency spatial gain noise in the camera, quantization error due to the finite number of DMD pixels that form one resolution element, and photon noise (in decreasing order of size).

In addition, the phase front of the output flattop beam was estimated by measuring the surface flatness of the DMD. A Michelson interferometric measurement showed 0.12 μm height variation at the portion of the DMD face used for beam shaping. Since the telescope system images both intensity and phase to the image plane, the measurement of DMD face flatness implies better than 0.8π phase flatness for the flattop beam.

3.2 *Incoherent Beam Shaping*

For incoherent beam shaping, we implemented two incoherent light sources: (1) 760 nm single-mode fiber pigtailed SLED (EXS7505-8411, EXALOS); (2) 781 nm single-mode fiber pigtailed laser diode (LPS-785-FC, Thorlabs). The pinhole was chosen to be one mm for the SLED and 0.8 mm for the laser diode. The experiment achieved 0.81% to 0.88% RMS flatness after refinement.[20] As an example, the cross sections of the raw measurement and the digitally low-pass filtered result of a flattop beam produced by the laser diode are displayed in Fig. 2. After digital low-pass filtering, the RMS error was reduced to 0.20% to 0.26% over the entire flattop beam (diameter = 1.32 mm).

We observed that there was a tradeoff between the source linewidth and energy conversion efficiency for the SLED. As a broad-band (20 nm) light source, SLED had less intensity non-uniformity by reducing speckle noise. However, it also introduces a broader spatial dispersion after the DMD that acts essentially as a diffraction grating. On the other hand, the spatial pinhole confines the system bandwidth as low as possible for high imaging accuracy (less than two nm). As a result, only a small fraction of the light can pass through the system, resulting in non-symmetric low-pass filtering as well as a significant energy loss. Even if the iterative pattern refinement was able to compensate the non-symmetric filtering effect, the severe energy loss excluded the SLED from high efficiency beam shaping applications.

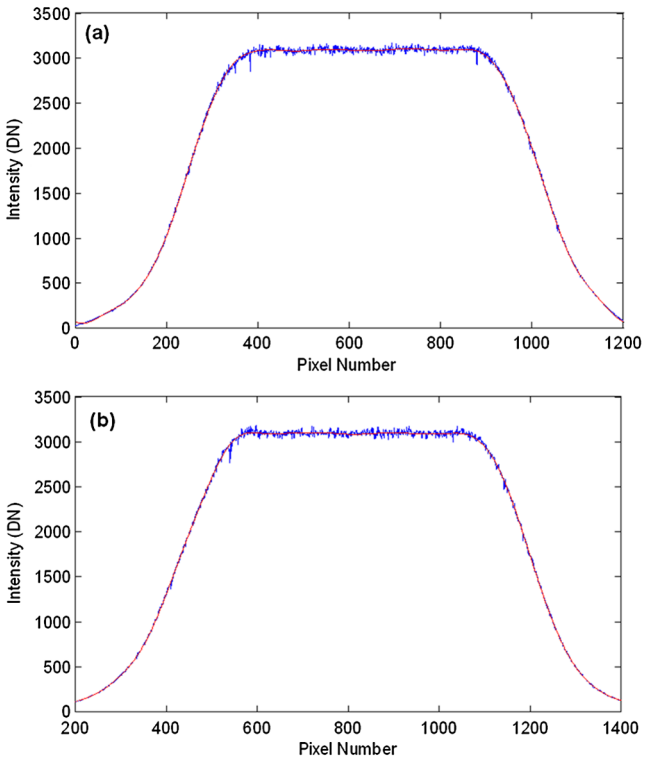

Fig. 2 Incoherent flattop beam shaping using a 781 nm laser diode. Vertical (a) and horizontal (b) cross sections of the camera image (blue) and digital LPF image (red).

3.3 *Comparison of Coherent and Incoherent Sources*

The data for RMS error for all the various light sources have been gathered in Table 1. The table compares the RMS error data over the entire flattop region for all four light sources, with and without the digital LPF. For the raw image, it is clear that coherent light sources produced more RMS error from speckle in the camera image. The 1064 nm SMF laser, which has the highest coherence, shows the largest intensity variance. On the other hand, both low-coherence light sources generated less than 0.9% RMS error, and the 760 nm SLED had the best intensity flatness and also the lowest coherence.

The RMS error decreased significantly after applying the digital LPF, illustrating that high spatial frequencies dominated the error in the raw camera image. The data for the 633 nm He-Ne laser was excluded from this analysis because the optical system was modified by changing the lens focal length, pinhole size, and therefore the radius of the digital LPF. In addition, this data was obtained after only five refinement iterations compared to 17 iterations for 1064 nm and 20 iterations for the SLED and laser diode. Thus, we expect more intensity variation in the output beam for the He-Ne laser experiments. For the other three light sources, we obtained similar RMS errors, ranging from 0.20% to 0.26%.

3.4 *Energy Conversion Efficiency*

The energy conversion efficiency depends upon DMD pixel mirror reflectivity (92%[21]), antireflection coating transmission of the DMD window, DMD fill factor (88%,[21] diffraction efficiency (depending on DMD mirror pitch and tilt angle, and the wavelength), and the user-selected loss in converting the input quasi-Gaussian to a flattop (typically 40% to 60% efficiency). For all light sources in the beam shaping experiment, the first three factors stay the same (as does the Gaussian-to-flattop conversion percentage). However, we observed that since the DMD functions as a blazed diffraction grating, operating away from the blaze angle resulted in significant energy loss.[22] The normalized diffraction efficiency is 73% for the 6th diffraction order at 633 nm and 53% for the 4th diffraction order at 1064 nm. Thus, neither operates near the diffraction peak. On the other hand, for the 781 nm laser diode, the diffraction efficiency increased drastically to nearly 100% (for 5th order) for a DMD tilt angle of 12°. The resulting overall conversion efficiency was calculated to be 21.2%. The measured result was 19.8%; almost three times larger than the 7% conversion measured at 1064 nm.[16] Therefore, we have shown that the 781 nm wavelength enhances the total energy efficiency for beam shaping.

If one wanted to maximize the conversion efficiency at 1064 nm for example, the DMD pixel pitch and window antireflection coatings need to be optimized. The pitch of the .55 XGA DLP chip of 10.8 μm has its 3rd order diffraction peak very close to 1064 nm. Unfortunately, this device is currently available with only visible AR coatings. So, either a custom window must be designed, or the standard IR window (from the other DLP chip configurations) would be used to replace the original window, but with a less-than-optimum total transmission of 78% for the standard IR window.

4 Homogeneous 1-D Optical Lattice Generation

The previous beam shaping experiments conducted at the imaging feedback arm have demonstrated high-precision flattop beams for various light sources that could be used to form either a standing-wave or thin optical lattice. Here

Table 1 RMS error in the whole flattop beam area for coherent and incoherent light sources.

Light sources		Coherent		Incoherent	
		633 nm He-Ne laser	1064 nm fiber laser	760 nm SLED	785 nm laser diode
Flattop diameter (mm)		1.36	1.50	1.32	1.32
Digital LPF[a]		1/32	1/96	1/71	1/90
RMS error (%)	Raw image	1.00	1.12	0.81	0.88
	LPF	0.67	0.23	0.26	0.20

[a]The radius of the digital LPF represents as the fraction of the maximum spatial frequency.

we report using beam shaping to generate a homogeneous 1-D standing-wave optical lattice of the correct dimensions for conducting cold atom experiments. Three of these identical systems, oriented orthogonally would be used to form a 3-D optical lattice. Several system requirements need to be considered for optical lattice generation. First, we must calculate the required input laser power because the depth of potential wells relates to the light intensity. Second, the quality of the flattop beam is sensitive to the camera gain non-uniformity and system alignment. Thus, an accurate system calibration is necessary to provide a uniform measurement base. Finally, the iterative refinement process was slow because it was operated off-line. Different software was used to control the camera, process the image, and load the DMD pattern. It was clear that integrated automation software should be used to increase the operation speed. Implementation of these objectives is described in the following sections.

4.1 *System Preparation*

We have chosen Rubidium-87 (^{87}Rb) atoms for our BEC experiment. A 1064 nm fiber laser is used to form the optical lattice. This wavelength is far away from the resonant frequency of Rubidium D1 ($5^2S_{1/2} \rightarrow 5^2P_{1/2}$) and D2 ($5^2S_{1/2} \rightarrow 5^2P_{3/2}$) transitions at 794 and 780 nm, respectively, but still maintains large enough optical dipole polarization to create a sufficient gradient force. In the BEC experiment, the dipole potential for standing wave needs to be much larger than the atom recoil energy, E_R, at the trapping laser wavelength in order to effectively confine atoms in the optical lattice. In our experiment, we would like to realize a dipole potential of $30E_R$, and this requires a laser intensity of $I = 496$ W/cm^2. For a 50×50 μm^2 flattop beam with the power conversion of 7%, the total power in the Gaussian beam is 1.26 W for 1-D optical lattice generation.

4.2 *System Calibration*

System calibration is needed before running a beam shaping experiment. Specifically, users need to complete camera calibration tasks: white field measurement, system alignment, scaling factor measurement (camera pixels to DMD pixels), and dark field subtraction.

First, white field measurement was conducted to correct for dust covered pixels and adjust the pixel gain. We placed an integrating sphere at the imaging plane of the image feedback arm. The output port was connected to the camera. In order to reduce the error introduced by photon noise and speckle interference, the low-pass filtered white field image was used to compensate the pixel gain non-uniformity. Then, we adjusted for dust-covered pixels by comparing the filtered image to the raw image, shown in Fig. 3. A selection algorithm was designed to compare the raw measurement to the low-pass filtered result for every pixel. If the difference was larger than the threshold (5% in the experiment), this pixel was considered as dust covered and the raw measurement intensity was replaced with the low-pass filtered image value.

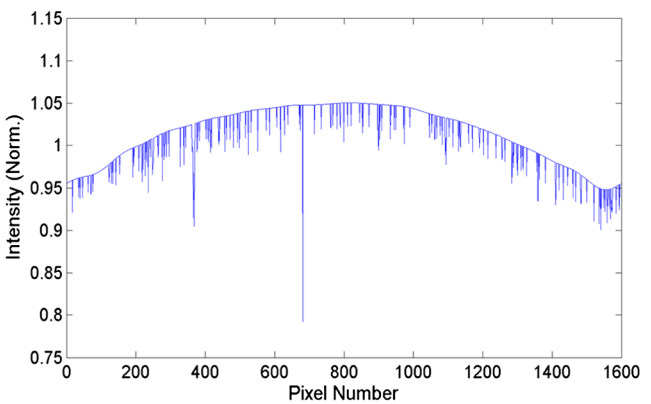

Fig. 3 Cross section of the LPF image of the white field measurement showing camera dust.

Second, we carefully aligned the camera perpendicular to the incident beam. This process removed interference fringes caused by reflection and scattering light in the CCD sensor. Third, the size-scaling factor between camera pixels and DMD pixels was measured to convert the measurement profile at the image plane back to the DMD plane for pattern generation and refinement. Finally, pixel intensity error caused by the dark current in the CCD sensor was subtracted by the Ultracal! Function[23] in the Spiricon laser beam profiler.

4.3 *Automation: LabVIEW Program Design*

In the early beam shaping experiments, different software was used to control the camera, process the image, and load the DMD pattern. A single beam measurement and pattern design iteration took 3 to 5 min, and 15 to 20 iterations were needed to arrive at a converged design. This greatly hindered the system operation speed. It was clear that integrated automation software should be used to increase the operation speed, and so a LabVIEW program was developed for this purpose. The automation program integrated image acquisition (Spiricon Laser Beam Profiler software), target-profile generation and refinement (Matlab), and DMD pattern loading (Discovery 1100 or 4000 DMD boards and drivers). Two similar user interfaces are used (shown in Fig. 4): first to obtain the initial DMD pattern and initial flattop beam, and second to control the iterative refinement of the beam. Before running the automated routine, users need to complete the system calibration tasks described in the previous section. After calibration, the LabVIEW-controlled system allowed fast and automated beam shaping experiments to be conducted. To reach the first flattop beam took 57 s, and to perform the iterative refinement took an additional 71 s.

4.4 *Lattice Beam Quality Measurement*

The optical lattice beam needs to have a 50×50 μm^2 flattop region to form a standing-wave optical lattice with ~100 lattice sites along each dimension. A two-stage imaging configuration is used in the optical lattice arm to reduce the size of the flattop beam from the DMD plane as shown in Fig. 1. For the first stage, a 100 mm focal length lens (f2) is paired with f1 to produce a $-1/5$ magnification telescope. This 5× reduced flattop beam is measured at the intermediate imaging plane. The beam is further reduced by another 100 mm focal length imaging lens (f4) to produce the optical lattice beam at the atoms plane. This lens is a doublet lens designed and AR coated for 780 to 1550 nm. Depending upon the beam size requirement, we adjusted f4 to achieve another 5 to 10 times reduction. Combined with the first stage, the size of the flattop beam is reduced by 25 to 50 times. In addition, we placed another beam splitter between

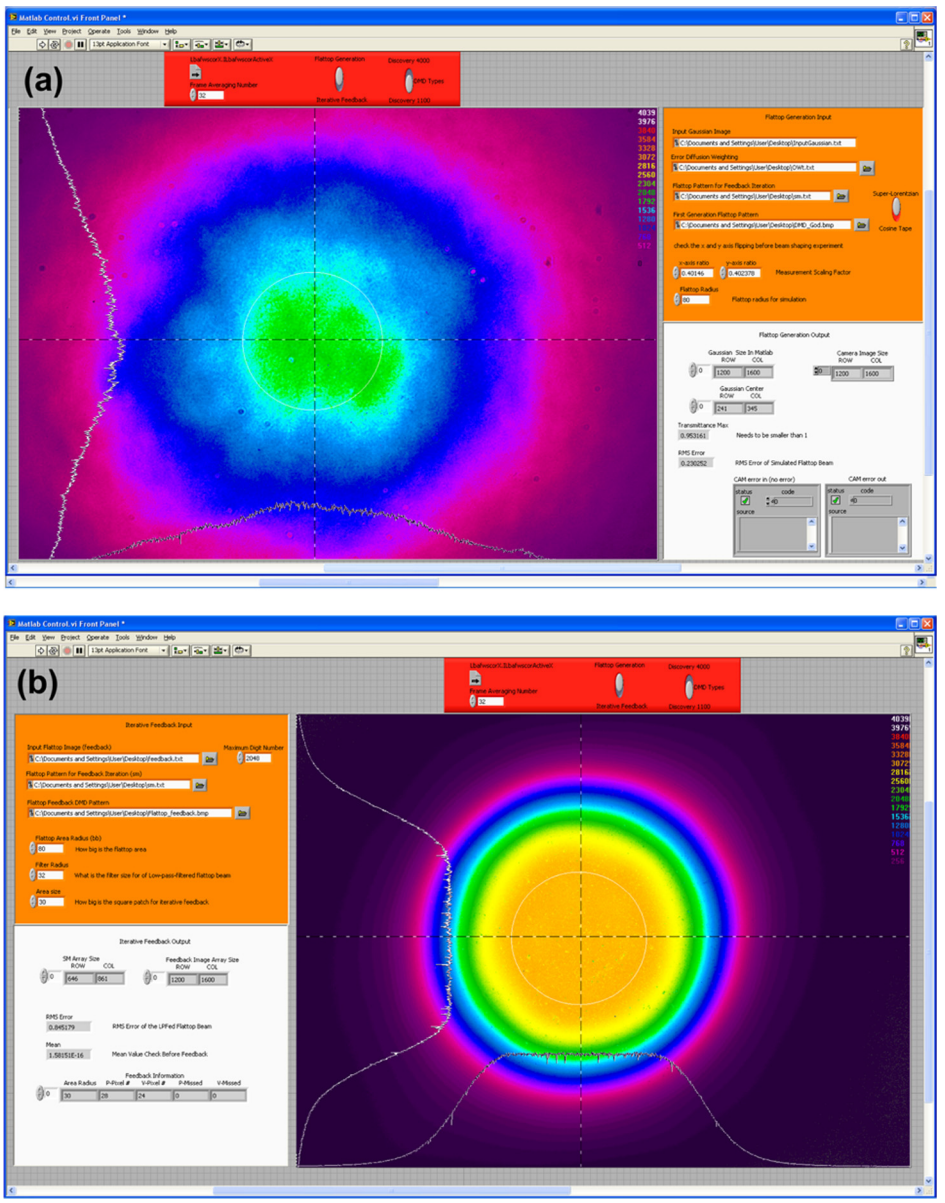

Fig. 4 LabVIEW interfaces for (a) flattop generation showing a typical input laser beam profile, and (b) iterative pattern refinement for the DMD-based high-precision beam shaper showing a typical flattop beam camera image.

f2 and f4 to create the third image plane that is equivalent to the intermediate imaging plane. This enables the measurement of the beam profile after retro-reflection and can be used to illustrate the beam quality of the optical lattice.

Beam profiles at various diagnostic planes were measured to examine the beam quality in the optical lattice arm. The raw RMS error for different measurement planes is summarized in Table 2. A flattop beam with RMS error of 1.15% was produced at the image feedback arm. In the optical lattice arm, measurement obtained 1.23% RMS error at the intermediate imaging plane. At the atoms' plane, the intensity uniformity was maintained at 1.25% RMS error over the entire circular flattop region with a diameter of 70.4 μm (Fig. 5). After retro-reflection, the intensity uniformity was slightly degraded to 1.40%. The measurement result demonstrated a high uniformity of the flattop beam at the optical lattice arm. Our calculation shows that the focal depth (Rayleigh range) at the atoms plane is ~50 μm. For a 1064 nm laser beam, this enables us to make ~100 lattice sites in the longitudinal dimension and is more than sufficient for the ultra-cold atoms experiment. Furthermore, the Phase Transfer Function (phase part of the optical transfer function or OTF) for a well-behaved imaging system (near diffraction limited and focused) is flat.[24] Thus the phase in the various image planes, including the atoms plane, will correspond to the phase of the wavefront leaving the DMD. The phase wavefront measurement using a Michelson interferometer showed that the phase difference over the central part of the DMD (flattop region) is $<0.77\pi$ in the horizontal direction and $<0.16\pi$ in the vertical direction.[16] Outstanding DMD face flatness over the flattop region assures the production of an output beam profile with good phase flatness.

The entire beam shaping system is evaluated by comparing beam profiles at different diagnostic planes. We first discuss the beam profile quality at the intermediate image plane (see Fig. 1) that is reduced by a factor of five from the

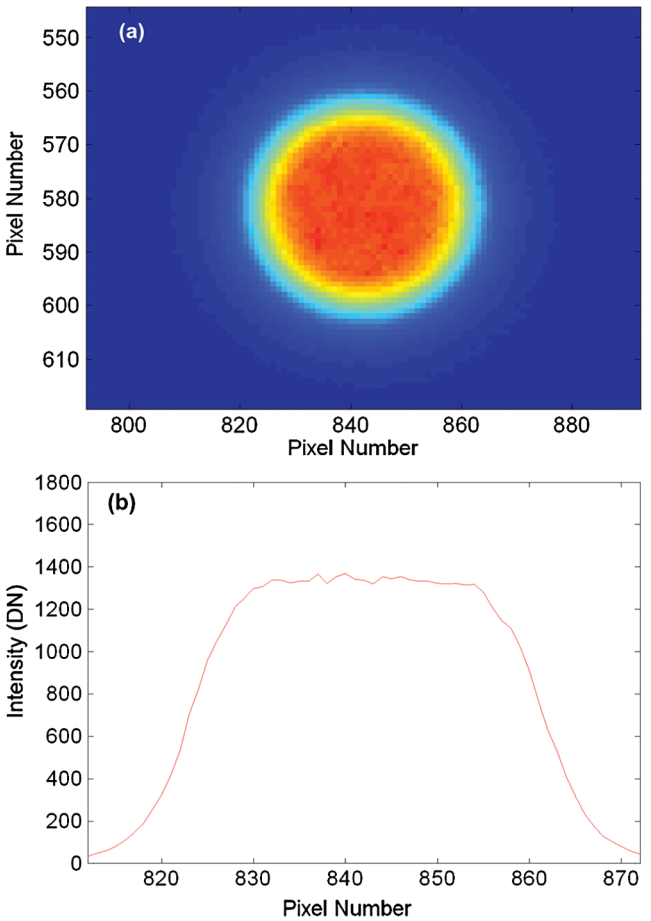

Fig. 5 (a) Top view and (b) cross section of the flattop beam profile at atoms plane.

DMD and is not in the iterative refinement loop. The raw intensity uniformity at the intermediate imaging plane (1.23%) slightly increased compared to the beam profile measured at the image feedback arm (1.15%). After the digital LPF, the RMS error also increased from 0.2% to 0.3% (image feedback plane) to 0.7% to 0.9% (intermediate imaging plane). For the Spiricon camera with a certain sampling rate (4.4 μm pixel width), smaller beam dimension brings in the intensity-averaging effect, which should compensate a 4-time increase of the digital LPF size due to change of the telescope configuration (from f1-f3 to f1-f2) in these two arms. This indicates that the beam profile after iterative pattern refinement has some non-uniformity to the optical lattice arm. This non-uniformity could possibly come from the aberration between different lenses (f2 and f3), error residual in system calibration, and other measurement error from the camera.

Second, we examine the evolution of beam profile quality at the atoms plane. The raw RMS error is essentially unchanged from the intermediate imaging plane to the optical lattice plane. Intensity uniformity after the digital low-pass filter is comparable as well. This result demonstrates that the single imaging lens (f4) does not further degrade the beam profile. In addition, the impact on the beam profile of the entire optical lattice arm is analyzed by comparing measurement results at the retro-reflected image plane to the intermediate imaging plane. The raw RMS error of the flattop beam increased by 0.17% after a round trip through the focusing and retro-reflection optics surrounding the atoms plane. This small degradation is mainly caused by various optical elements in the optical lattice arm. Thus, we have demonstrated that the optical lattice arm has little impact on the beam quality. The experiment verifies that this system was capable of producing a high-quality flattop beam profile through the optical lattice volume both for the incident and retro-reflected beams.

The system evaluation concludes that the main error residue of the flattop beam at the optical lattice arm is still from the intensity non-uniformity of the beam profile, and it is caused by the non-equivalent performance of beam shaping between the image feedback arm and the optical lattice arm. For the future, we propose to conduct further pattern refinement based on measurements of the cold atom distribution, which is even more sensitive to small variations in the optical field. This approach should remove most RMS residue and improve intensity uniformity of the optical lattice beam.

5 Summary

In conclusion, we demonstrated that a precise flattop laser beam could be generated and retro-reflected while maintaining its flattop quality. In a cold atoms experiment, atoms placed at the coincident focus of both the incident and retro-reflected beams will experience a standing wave optical field that has a mean intensity of a precise flattop. This beam shaping system converts a quasi-Gaussian input beam to a flattop beam with high accuracy. In the image feedback arm, the beam shaping experiments using various coherent and incoherent light sources achieve 0.81% to 1.12% RMS error over the entire flattop region of a raw camera image. Speckle interference and noise dominates the intensity non-uniformity. The digital low-pass filter equivalent to pinhole size in the experiment was designed to reveal the intensity flatness of the actual beam profile by eliminating any high-spatial frequency noise in the camera. The RMS error was reduced to 0.2% to 0.26% after the digital low-pass-filter was applied for all light sources. In addition, we analyzed the relation between the diffraction efficiency and operation wavelength. Light sources close to the blaze wavelength of the DMD enhanced the diffraction efficiency. The best possible power conversion efficiency with 40% Gaussian-to-flattop conversion was 20% to 26%.

Table 2 Raw RMS error of measurement flattop beam in various diagnostic planes.

Measurement plane	Image feedback	Intermediate	Optical lattice	Retro-reflected
Flattop dia. (μm)	1760	352	70.4	352
Raw RMS error (%)	1.15	1.23	1.25	1.40

The energy requirement for a 1-D standing-wave optical lattice was calculated for a 1064 μm laser beam. A LabVIEW automated program was designed to achieve fast on-line flattop generation using the iterative refinement process. In addition, various system calibrations were conducted to improve the measurement accuracy. The size of the flattop beam was reduced by a factor of 25 to 50 by the telescope followed by an imaging lens. At the atoms' plane, we produced a 1.25% RMS error circular flattop beam with diameter of 70.4 μm. This beam was retro-reflected to form the optical lattice at the atoms plane. The measurement of the retro-reflected beam profile illustrated a good intensity uniformity at the optical lattice. These results indicate that the generated homogeneous 1-D optical lattice is sufficient for use in a quantum emulator using ultracold atoms.

Acknowledgments

This work was supported by a grant from the Army Research Office with funding from the Defense Advanced Research Projects Agency (DARPA) Optical Lattice Emulator Initiative (OLE) program.

References

1. J. H. Denschlag et al., "A Bose-Einstein condensate in an optical lattice," *J. Phys. B: Atom. Mol. Opt. Phys.* **35**(14), 3095–3110 (2002).
2. M. Greiner et al., "Quantum phase transition from a superfluid to a Mott insulator in a gas of ultracold atoms," *Nature* **415**(6867), 39–44 (2002).
3. J. K. Chin et al., "Evidence for superfluidity of ultracold fermions in an optical lattice," *Nature* **443**(7114), 961–964 (2006).
4. W. S. Bakr et al., "A quantum gas microscope for detecting single atoms in a Hubbard-regime optical lattice," *Nature* **462**(7269), 74–77 (2009).
5. M. G. Tarallo et al., "Generation of a flattop laser beam for gravitational wave detectors by means of a nonspherical Fabry-Perot resonator," *Appl. Opt.* **46**(26), 6648–6654 (2007).
6. D. Grewel and A. Benatar, "Diffractive optics as beam-shaping elements for plastics laser welding," *Opt. Eng.* **46**(11), 118001 (2007).
7. J. H. Kelly et al., "OMEGA EP: high-energy petawatt capability for the OMEGA laser facility," *J. Phys. IV* **133**(1), 75–80 (2006).
8. C. Dorrer, "High-damage-threshold beam shaping using binary phase plates,"*Opt. Lett.* **34**(15), 2330–2332 (2009).
9. R. de Saint Denis et al., "Beam-shaping longitudinal range of a binary diffractive optical element," *Appl. Opt.* **45**(31), 8136–8141 (2006).
10. Z. Sun and H. K. Kim, "Refractive transmission of light and beam shaping with metallic nano-optic lenses," *Appl. Phys. Lett.* **85**(4), 642–644 (2004).
11. J. A. Hoffnagle and C. M. Jefferson, "Design and performance of a refractive optical system that converts a Gaussian to a flattop beam," *Appl. Opt.* **39**(30), 5488–5499 (2000).
12. C. Dorrer and J. D. Zuegel, "Design and analysis of binary beam shapers using error diffusion," *J. Opt. Soc. Am. B* **24**(6), 1268–1275 (2007).
13. V. Bagnoud and J. D. Zuegel, "Independent phase and amplitude control of a laser beam by use of a single-phase-only spatial light modulator," *Opt. Lett.* **29**(3), 295–297 (2004).
14. L. Hu et al., "Phase-only liquid crystal spatial light modulator for wavefront correction with high precision," *Opt. Express* **12**(26), 6403–6409 (2004).
15. J. Liang et al., "1.5% root-mean-square flat-intensity laser beam formed using a binary-amplitude spatial light modulator," *Appl. Opt.* **48**(10), 1955–1962 (2009).
16. J. Liang et al., "High-precision laser beam shaping using a binary-amplitude spatial light modulator," *Appl. Opt.* **49**(8), 1323–1330 (2010).
17. S. Sumriddetchkajorn, "Micromechanics-based digitally controlled tunable optical beam shaper," *Opt. Lett.* **28**(9), 737–739 (2003)
18. V. Ostromoukhov, "A simple and efficient error-diffusion algorithm," in *Proc. SIGGRAPH*, ACM, New York, NY, USA, pp. 567–572 (2001).
19. M. F. Becker et al., "High-precision laser beam shaping using binary-amplitude DLP spatial light modulators," *Proc. SPIE* **7596**, 75960A (2010).
20. J. Liang et al., "High-precision beam shaper for coherent and incoherent light using a DLP spatial light modulator," *Proc. SPIE* **7932**, 793208 (2011).
21. Texas Instrument, "DMD 0.7 XGA 12° DDR DMD Discovery™ Datasheet," http://focus.ti.com/download/dlpdmd/2503686.pdf (accessed 31 1 2012).
22. J. P. Rice et al., "DMD diffraction measurements to support design of projectors for test and evaluation of multispectral and hyperspectral imaging sensors," *Proc. SPIE* **7210**, 72100D (2009).
23. Ophir-Spiricon, LLC, "LBA-FW-SCOR User Manual," pp. 98–99 http://www.ophiropt.com/laser/register_files/lbafwscor.pdf (accessed 18 3 2011).
24. J. Goodman, *Introduction to Fourier Optics*, Chapter 6, Roberts and Company Publishers, Greenwood Village, Colorado, pp. 135–145 (2004).

Jinyang Liang is currently a doctoral candidate and graduate research assistant in the Department of Electrical and Computer Engineering at the University of Texas at Austin (UT). He received his BE in photoelectric engineering from Beijing Institute of Technology, Beijing, China in 2007, and his MSE in electrical engineering from UT in 2009. His research interests mainly focus on optical signal processing using modulation optical devices, including high-precision beam shaping, holographic image projection, and quantum emulation using ultra-cold atoms. He is a student member of the SPIE and the OSA.

Rudolph Kohn is a doctoral candidate and graduate research assistant in the Physics Department of the University of Texas at Austin. He received his BS in physics from the University of Michigan in Ann Arbor in 2006. His research focuses on the creation and control of clouds of ultracold Rubidium atoms.

Michael F. Becker is a professor in the Department of Electrical and Computer Engineering at The University of Texas at Austin, and holds the William H. Hartwig Fellowship in electrical engineering. He received his BES from The Johns Hopkins University, Baltimore, MD, in 1969, and the MS and PhD degrees from Stanford University, Stanford, CA, in 1970 and 1974, respectively, all in electrical engineering. He was an associate (visiting) professor at l'Institut d'Optique, Faculty of Physics, at the University of Paris-11 at Orsay France in 1993 and at the engineering school Ecole Centrale de Lille, France, in 1999. His current research includes laser applications to material processing, nanoparticle generation and application, laser damage, nano-sized optical elements, nonlinear optics, and optical signal processing. He is a Senior Member of the IEEE and a member of Sigma Xi, Tau Beta Pi, the Optical Society of America, and SPIE.

Daniel J. Heinzen is a professor in the Department of Physics at The University of Texas at Austin, and holds the Fondren Centennial Foundation Chair in Physics. He received his BS and PhD from Massachusetts Institute of Technology. His research interests include ultracold atomic sources and collisions, quantum gases and quantum emulation, and atomic and molecular physics tests of fundamental symmetries. He is a fellow of the American Physical Society.